Numerical Analysis of the Internal Kinematics and Dynamics of 3D Breaking Waves on Slopes

Benjamin Biausser[1], Stéphan T. Grilli[2], Philippe Fraunié[1], and Richard Marcer[3]

1. LSEET-LEPI
Université de Toulon et du Var
La Garde, France

2. Dept. of ocean Engineering
University of Rhode Island
Narragansett 02882 RI, USA

3.PRINCIPIA R.D.
La Ciotat, France

ABSTRACT

In this paper, we describe the development and validation of a numerical model based on coupling a higher-order Boundary Element Method (BEM) solution of fully nonlinear potential flow equations to a Volume Of Fluid (VOF) solution of Euler equations, in three-dimensions (3D). The BEM solution is used as an initialization of the VOF/Navier-Stokes solver. Numerical simulations of breaking waves on sloping beaches for 2D (using an earlier similar model) and 3D flows are carried out. Finally, we simulate the breaking and post-breaking of a solitary wave over a sloping ridge in a three-dimensional numerical wave tank. Analysis of wave profiles and internal kinematics (velocity, vorticity, pressure) are presented.

KEY WORDS: breaking ocean waves; nonlinear surface waves; Boundary Element Method; Segment Lagrangian Volume of Fluid Method; numerical wave tank; three-dimensional flows.

INTRODUCTION

The study of breaking waves is of prime importance in many ocean and naval engineering applications, such as air-sea interactions or sediment transport, and the prediction of damages caused by storms to ocean and naval structures. Despite significant progress in recent years, our understanding of wave breaking dynamics and kinematics is still quite incomplete. Due to recent improvements in computer performances, direct Computational Fluid Dynamics (CFD) simulations of wave breaking can now be carried out and used to gain insight into these complex processes. In such problems, one numerically solves full fluid dynamics equations, together with nonlinear dynamic and kinematic free surface boundary conditions, and other boundary conditions specifying solid surfaces or open boundaries. Such computations, however, are still very demanding over large computational domains. Models based on potential flow equations (Boundary Element Methods i.e. BEM) are very accurate and efficient for simulating wave shoaling over arbitrary bottom topography, up to overturning (Grilli et al., 1994, 1996, 1997, and 2001). Such models, however, cannot simulate interface reconnections, large deformations, and vorticity, occurring during wave breaking. To combine the advantages of both approaches, Guignard et al. (1999) proposed to use a BEM solution as an initial solution for a VOF/Navier-Stokes (or Euler) model, in which wave breaking could be fully simulated. More specifically, the VOF interface tracking method is less numerically accurate and much more computationally intensive than the Boundary Integral Equations Method (BIEM) of Grilli et al., for wave shoaling, but it allows to simulate breaking and post-breaking stages. Moreover, after breaking occurs, the flow becomes rotational so that potential theory becomes invalid. This is the reason why the coupling between the BIEM and VOF/Navier-Stokes solver is achieved. These coupled BEM/VOF computations have so far been performed in 2D (Guignard et al., 1999). Here, we apply the same approach to 3D problems, through coupling of Grilli et al.'s (2001) 3D-BEM model to the interface tracking, SL-VOF 3D method of Biausser et al. (2004).

In the first section, the mathematical formulation is briefly presented. The second section deals with the numerical methods, with details of the interface tracking SL-VOF method, and coupling with the BEM formulation for wave breaking. Then, a simple application of quasi-2-D wave breaking simulation with the 3D-BEM/SL-VOF model is presented for validation. Finally, the case of a solitary wave overturning and breaking over a 3D sloping bottom is analyzed in the last section.

MATHEMATICAL FORMULATION

BEM formulation

Equations for fully nonlinear potential flows (FNPF) with a free surface are listed below. The velocity potential $\phi(\mathbf{x},t)$ is introduced to describe inviscid irrotational 3D flows, in Cartesian coordinates $\mathbf{x} = (x,y,z)$, with z the vertical upward direction (z=0 at the undisturbed free surface), and the fluid velocity is expressed as $\mathbf{u} = \nabla\phi$. Continuity equation in the fluid domain $\Omega(t)$ with boundary $\Gamma(t)$ reads

$$\nabla^2 \phi = 0. \qquad (1)$$

The corresponding three-dimensional free-space Green's function is defined as,

$$G(\mathbf{x},\mathbf{x}_l) = \frac{1}{4\pi r} \qquad \text{with} \qquad \frac{\partial G}{\partial n}(\mathbf{x},\mathbf{x}_l) = -\frac{1}{4\pi}\frac{\mathbf{r}.\mathbf{n}}{r^3}, \tag{2}$$

with, $r = |\mathbf{x} - \mathbf{x}_l|$ the distance from the source point $\mathbf{x}$ to the field point $\mathbf{x}_l$ (both on boundary Γ), and $\mathbf{n}$ the outward unit vector normal to the boundary at point $\mathbf{x}$. Green's second identity transforms Eq. (1) into the Boundary Integral Equation (BIE)

$$\alpha(\mathbf{x}_l)\phi(\mathbf{x}_l) = \int_\Gamma \left[\frac{\partial \phi}{\partial n}(\mathbf{x})G(\mathbf{x},\mathbf{x}_l) - \phi(\mathbf{x})\frac{\partial G}{\partial n}(\mathbf{x},\mathbf{x}_l)\right] d\Gamma \tag{3}$$

The boundary is divided into various parts in which different boundary conditions are specified. On the free surface $\Gamma_f(t)$, ϕ satisfies the nonlinear kinematic and dynamic boundary conditions,

$$\frac{D\mathbf{R}}{Dt} = \mathbf{u} = \nabla\phi \quad , \tag{4}$$

$$\frac{D\phi}{Dt} = -gz + \frac{1}{2}\nabla\phi.\nabla\phi - \frac{p}{\rho} \quad , \tag{5}$$

respectively, in a Mixed Eulerian-Lagrangian formulation (MEL), with $\mathbf{R}$ the position vector of a fluid particle on the free surface, g the acceleration due to gravity, p the atmospheric pressure, ρ the fluid density and $D/Dt = \partial/\partial t + \nabla\phi.\nabla$ the Lagrangian time derivative. The effects of surface tension are neglected.

For simple waves, such as solitary waves, the free surface shape, potential and normal velocity of the incident wave are specified at time $t = 0$ on the free surface based on Tanaka's method (Tanaka,1986). [This method very accurately solves FNPF equations.] More complex incident wave conditions can be specified using numerical wavemakers (e.g., Grilli and Horrillo, 1997, 1999; Brandini and Grilli, 2001). On the bottom boundary, Γ_b and on other fixed parts of the boundary, a no-flow condition is prescribed as,

$$\frac{\partial \phi}{\partial n} = 0. \tag{6}$$

Once the BIE (3) is solved, the solution within the domain can be explicitly calculated, based on boundary values. Using Eq. (3), for instance, the internal velocity at the interior point $\mathbf{x}_i$ is given by Eqs. (7) and (8), respectively, below

$$\mathbf{u}(\mathbf{x}_i) = \nabla\phi(\mathbf{x}_i) = \int_\Gamma \left[\frac{\partial \phi}{\partial n}(\mathbf{x})Q(\mathbf{x},\mathbf{x}_i) - \phi(\mathbf{x})\frac{\partial Q}{\partial n}(\mathbf{x},\mathbf{x}_i)\right] d\Gamma, \tag{7}$$

$$Q(\mathbf{x},\mathbf{x}_i) = \frac{1}{4\pi r^3}\mathbf{r}, \quad \frac{\partial Q}{\partial n}(\mathbf{x},\mathbf{x}_i) = \frac{1}{4\pi r^3}\left[\mathbf{n} - 3(\mathbf{r}.\mathbf{n})\frac{\mathbf{r}}{r}\right], \tag{8}$$

where r denotes the distance from the boundary point $\mathbf{x}$ to $\mathbf{x}_i$.

Navier-Stokes (or Euler) Formulation

The 3D Navier-Stokes equations for two-phase (air-water) flows are given as follows, in a semi-conservative curvilinear formulation,

$$\frac{1}{J}\frac{\partial W}{\partial t} + \frac{\partial F}{\partial \xi} + \frac{\partial G}{\partial \eta} + \frac{\partial H}{\partial \chi} = \frac{R}{J} + \frac{T}{J} \tag{9}$$

where F, G and H are flux terms, R is the volumetric force source term and T the surface tension source term, with,

$$F = \frac{1}{J}\begin{pmatrix} \rho\tilde{u} \\ \rho\tilde{u}u + \xi_x p - \vec{\nabla}(\xi).\vec{\tau}_x \\ \rho\tilde{u}v + \xi_y p - \vec{\nabla}(\xi).\vec{\tau}_y \\ \rho\tilde{u}w + \xi_z p - \vec{\nabla}(\xi).\vec{\tau}_z \end{pmatrix}; G = \frac{1}{J}\begin{pmatrix} \rho\tilde{v} \\ \rho\tilde{v}u + \eta_x p - \vec{\nabla}(\eta).\vec{\tau}_x \\ \rho\tilde{v}v + \eta_y p - \vec{\nabla}(\eta).\vec{\tau}_y \\ \rho\tilde{v}w + \eta_z p - \vec{\nabla}(\eta).\vec{\tau}_z \end{pmatrix};$$

$$H = \frac{1}{J}\begin{pmatrix} \rho\tilde{w} \\ \rho\tilde{w}u + \chi_x p - \vec{\nabla}(\chi).\vec{\tau}_x \\ \rho\tilde{w}v + \chi_y p - \vec{\nabla}(\chi).\vec{\tau}_y \\ \rho\tilde{w}w + \chi_z p - \vec{\nabla}(\chi).\vec{\tau}_z \end{pmatrix}; W = \begin{pmatrix} 0 \\ \rho u \\ \rho v \\ \rho w \end{pmatrix}; T = \begin{pmatrix} 0 \\ \sigma K n_x \\ \sigma K n_y \\ \sigma K n_z \end{pmatrix}; R = \begin{pmatrix} 0 \\ \rho f_x \\ \rho f_y \\ \rho f_z \end{pmatrix}$$

$$\tilde{u} = \xi_x u + \xi_y v + \xi_z w\,;\ \tilde{v} = \eta_x u + \eta_y v + \eta_z w\,;\ \tilde{w} = \chi_x u + \chi_y v + \chi_z w\,;$$

$$J = \frac{\partial(\xi,\eta,\chi)}{\partial(x,y,z)}$$

$$\vec{\tau}_x = \bar{\bar{\tau}}.\vec{e}_x \quad \vec{\tau}_y = \bar{\bar{\tau}}.\vec{e}_y \quad \vec{\tau}_z = \bar{\bar{\tau}}.\vec{e}_z \quad \bar{\bar{\tau}} = \mu(\vec{\nabla}\vec{U} + \vec{\nabla}^t\vec{U}) \tag{10}$$

where (ξ,η,χ) denote curvilinear coordinates, J is the Jacobian matrix of the coordinate transformation, σ is the surface tension coefficient, K the surface curvature and $\vec{n} = (n_x, n_y, n_z)$ the normal vector to the interface. Additionally, (u,v,w) are the Cartesian velocity components for each phase, $(\tilde{u},\tilde{v},\tilde{w})$ the contravariant velocity components, p the pressure, ρ the density, μ the molecular viscosity, and $\bar{\bar{\tau}}$ the viscous stress tensor. In the present applications, molecular viscosity will be neglected so that actually Euler equations are solved. Taking into account molecular viscosity for the kind of meshes used here in fact would not impact results significantly (this was verified in applications). To model viscous effects in computations, one should use refined meshes, but then computational times would considerably increase. The other standard option would be to use a turbulence model, which was not done here. Surface tension effects are also neglected for those applications. The Euler model used allows for including surface tension terms, but in our case, considering the physical scales involved, surface tension effects were found negligible.

NUMERICAL MODELS

Numerical method for the BIEM model

A second-order explicit scheme based on Taylor series expansions is used to update the position R and velocity potential ϕ on the free surface. A high-order Boundary Element Method (BEM) is used to solve numerically the BIEs for ϕ and $\partial\phi/\partial t$ (Grilli et al., 2001). The boundary is discretized into collocation nodes, defining two-dimensional elements for local interpolations of the solution in between these nodes. Within each element, the boundary geometry and field variables are interpolated using cubic polynomial shape functions (the boundary elements are 4x4-node quadrilaterals associated with bi-cubic shape functions of which only the middle quadrilateral is used). The discretized boundary integrals are evaluated for each collocation node by numerical integration. A special treatment is applied for weakly singular integrals. As the linear algebraic system resulting from the discretization of BIE (3) is in general dense and non-symmetric, a generalized minimal residual (GMRES) algorithm with preconditioning is used to solve it (Xü & Yue, 1992). Accuracy is increased in regions of high variability by

redistributing nodes using a regridding technique based on the BEM shape functions.

Numerical method for the VOF/Navier-Stokes model

Time discretization for the Navier-Stokes model is ensured using a fully implicit second-order scheme. The solution of the non-linear system for the unknown values at step n+1 is based on the pseudo-compressibility method (Viviand 1980, De Jouëtte et al. 1991), in which a time-like variable τ, called pseudo-time is introduced. Thus, in Eq. (9), we add pseudo-unsteady terms, which are derivatives of the unknowns at time level n+1, with respect to τ. These pseudo-density terms involve a new unknown $\tilde{\rho}$, called pseudo-density, which is constrained to remain positive. The pressure is calculated as a function of $\tilde{\rho}$, through an additional pseudo-state equation,

$$p^{n+1} = \rho(U_0^2 + \lambda U_n^2)\ln\left(\frac{\tilde{\rho}}{\rho}\right)^{n+1} \qquad (11)$$

The choice of an optimal pseudo-state equation is discussed in Viviand (1995).

Interface tracking VOF method. The VOF method (Hirt and Nichols, 1981) uses the volumetric fraction C of the denser fluid in grid cells, to track interface locations. This method is very efficient for tracking highly deformed interfaces. Unlike the BEM method, the VOF method can deal with topological reconnections or de-connections. More specifically, we use the Segment Lagrangian Volume Of Fluid method (SL-VOF; Guignard et al. 1999, Biausser et al. 2001,2004), for 2D and 3D flows, which is based on a piecewise linear modeling of the interface (PLIC) and a Lagrangian advection scheme. At the beginning of a time step, say n, the VOF field C is used to define a piecewise linear interface representation (segments in 2D or portions of planes in 3D). To do so, in each computational cell, the normal vector **n** to the interface plane, defined as $-\nabla C^n$, is first evaluated using finite differences. Once this direction is known, the segment is translated in the cell in order to satisfy the VOF cell value. Lagrangian markers M_i are specified on each segment/plane and, in each cell, these are advected based on the flow velocity computed in the Navier-Stokes solver. The segment corner/edge velocities are calculated from the velocity at the center of each cell using bilinear interpolation. The advection is carried out with a first order Lagrangian scheme

$$\mathbf{x}(t+\Delta t) = \mathbf{x}(t) + \Delta t\, \mathbf{u}\,, \qquad (16)$$

where **x** denotes the segment/plane corner/edge position, **u** the corner/edge velocity and Δt the time step. To each marker M_i, we associate the normal vector $\mathbf{n}_i$ of the segment/plane, to which the marker belongs. After advection, we find two possible types of cells: (i) A type cells containing at least one marker; (ii) B type cells without any marker.

Let us consider an A type cell (Fig. 1). To the marker M_i corresponds a value C_i calculated according to the PLIC method. As there are several portions of segments (for 2D cases) in the cell, it is necessary to determine whether the cell is growing full (interface reconnection) or not. To do so, a test is made on the value of, $pr_{ij} = \mathbf{n}_i.\mathbf{n}_j$, where i and j describe the markers present in the cell. If all the pr_{ij}'s are positive, then the new value of the VOF field C will be the mean of the C_i's in the cell, to which is added or subtracted the areas of additional polygons A(T). If at least one pr_{ij} is negative, a reconnection of interfaces could occur in the cell. Thus, segments could overlap with each other, so that the cell would become full of liquid phase. This is the case when the sum of the C_i's is greater than 1, and C^{n+1} is then specified to be 1 (Fig. 2). If the sum of the C_i's is less than 1, C^{n+1} is computed in the same way as above.

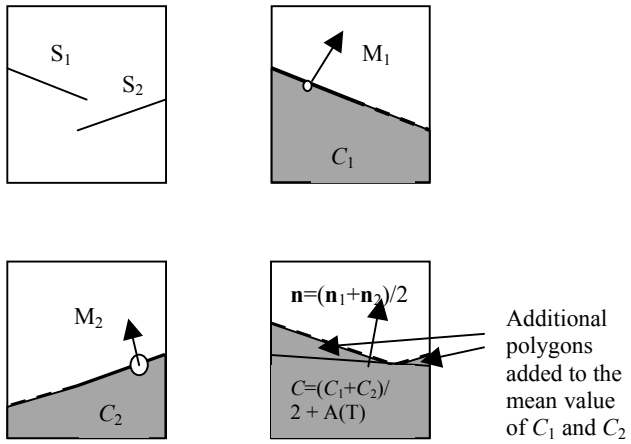

Fig. 1: computation of C^{n+1} for an A type cell with 2 segments (no reconnection). S_1 defines C_1, S_2 defines C_2, C is the mean value of C_1 and C_2, plus the areas of the additional triangles

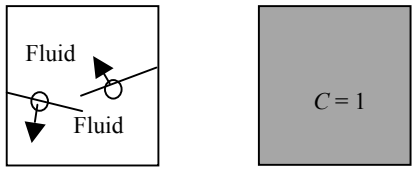

Fig. 2: computation of C^{n+1} for a A type cell with 2 segments (reconnection)

Let us now consider a B type cell (Fig. 3). There are again two possibilities: (i) either the cell did not contain any segment before advection of the interface, and thus the value of C is not modified; (ii) or the cell has lost its interface during the current time step. In case (ii), one has to detect whether the cell becomes empty or full of the denser fluid, after advection. A test is made on the value of, pr = **n.d** where **d** is the displacement of the center of the segment during advection. The cell is deemed full if pr > 0 and empty if not (Fig. 3).

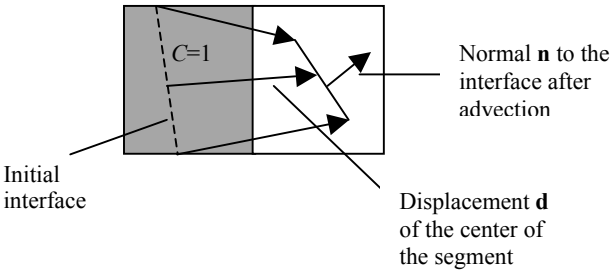

Fig. 3: computation of C^{n+1} for a B type cell case with, $\mathbf{n}.\mathbf{d} > 0$

For 3D problems, the principle of the method remains the same but the geometrical relationships are more complex and based on the motion of planes rather than segments (see Biausser et al., 2004). The piecewise linear modelling of the interface again makes it possible to track interfaces with complex and/or distorted shape with good accuracy. The Lagrangian advection performed in cells in 2D or 3D allows us to use large values of the Courant number (CFL), which reduces computational time.

NUMERICAL RESULTS

In this section, the two numerical models described above are used together to compute the shoaling and breaking of a solitary wave over a sloping bottom (2D) and then over a sloping ridge (3D). The BEM model is used to compute initial wave shoaling transformations, up to close to the breaking point. Laboratory experiments showed that potential flow theory is very accurate to describe such wave transformations (Grilli et al., 1994, 1997). When the wave front face reaches a large angle, the BEM solution is used to initialize the Navier-Stokes (Euler)/VOF model, both for free surface/interface geometry and internal velocity and pressure fields at VOF cell centers. The second part of the simulation i.e. overturning, breaking and post-breaking, is then computed with the VOF method, by solving Euler equations (i.e., viscosity is neglected). The air phase dynamics is neglected in this case to limit computational time.

Breaking of a solitary wave over a sloping bottom

We compute the breaking of a solitary wave induced by a sloping bottom, as occurs for ocean waves on most beaches, i.e., a quasi-2D problem, which we solve as a 3D problem, in order to validate the VOF model. Here, the transfer from potential to kinetic energy during wave shoaling, causes breaking through reducing depth, rather than non-physical initial conditions used in some earlier similar studies (Lubin et al., 2003).

We thus model a 3D domain, with a constant depth region followed by a sloping bottom (Fig. 4). Two sub-domains are considered, the first one corresponding to the flat bottom, from $x = 0$ to $x = 14$ m (with depth $h_0 = 1$ m), and the second one corresponding to a 1 : 15 slope from $x = 14$ m to $x = 35$ m, where wave shoaling occurs, eventually causing breaking. Based on earlier work (Grilli et al., 1997), for incident solitary waves, breaking wave characteristics depend on both initial wave height and on bottom slope. Let H_0 be the initial wave height and $H_0' = H_0/h_0$. The initial wave geometry and free surface kinematics are calculated based on Tanaka's (1986) method, as an exact FNPF solitary wave of height $H_0' = 0.5$, with its crest initially located at $x = 8.5$ m (Fig. 4). Such a wave would propagate without change of form in the BEM model, over constant depth (Grilli et al., 1994, 1997). In this application, however, no propagation is computed in the BEM model, which is only used to generate the initial conditions, within the 3D sub-domain of constant depth, for the VOF/Navier Stokes solver. These are velocity (using Eqs. 7,8) and pressure fields (using Bernoulli equation), corresponding to the specified solitary wave geometry and free surface kinematics.

As explained above, the VOF/Navier-Stokes solver is used here to compute the full shoaling and breaking of the wave. Viscous effects are neglected; hence Euler equations are solved rather than Navier-Stokes'. As previously discussed, breaking occurs as a result of shoaling over a non-uniform bottom topography. Fig. 5 shows, the wave progressively overturns, reaching the breaking point (where the crest front face becomes vertical) at $x = 27$ m. Eventually, a large size breaker jet is projected forward, producing a plunging type breaker. The breaking wave height, 0.45 m, is slightly smaller than predicted by the (experimentally validated) BEM model (Grilli et al., 1994, 1997). This reduction is due to numerical diffusion occurring in the Euler solver over long simulation times: since the air phase was neglected, to limit computational time, the physical fields must be interpolated on the free surface, which leads to unwanted loss of energy, and then to amplitude loss.

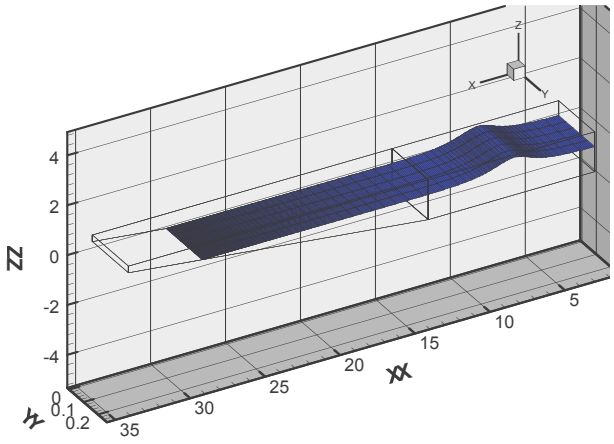

Fig. 4 : Initial conditions and computational domain for solitary wave shoaling and breaking over a 1:15 slope ($H_0' = 0.5$).

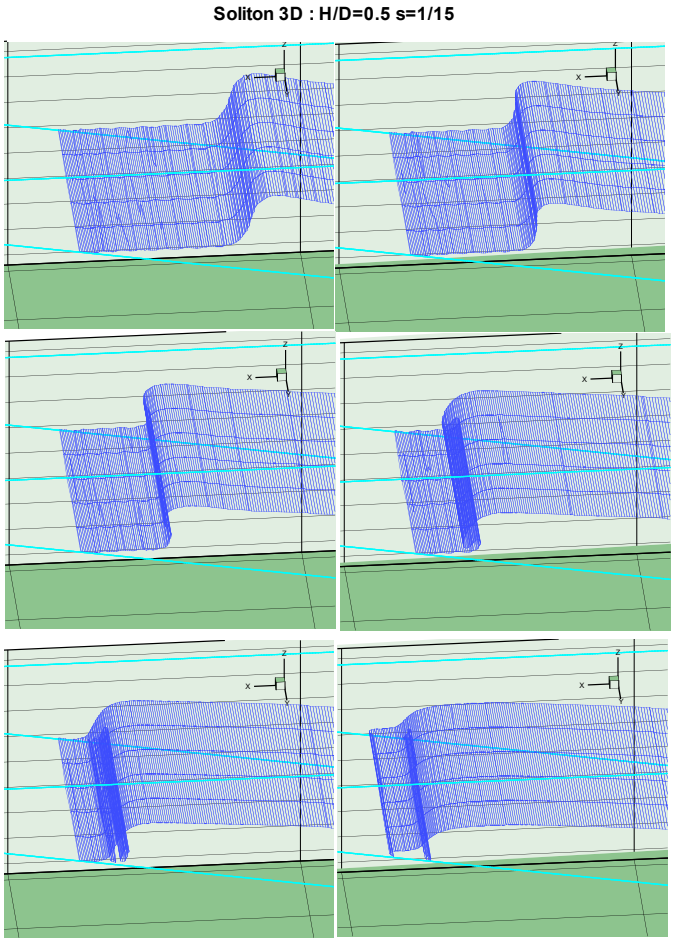

Fig. 5: breaking of a solitary wave over a sloping 1:15 slope (case of Fig. 6, with $H_0' = 0.5$).

This loss of wave energy during shoaling can be reduced by initializing the VOF model closer to the breaker point, and thus by

computing most of the shoaling transformations with the BEM rather than the VOF model.

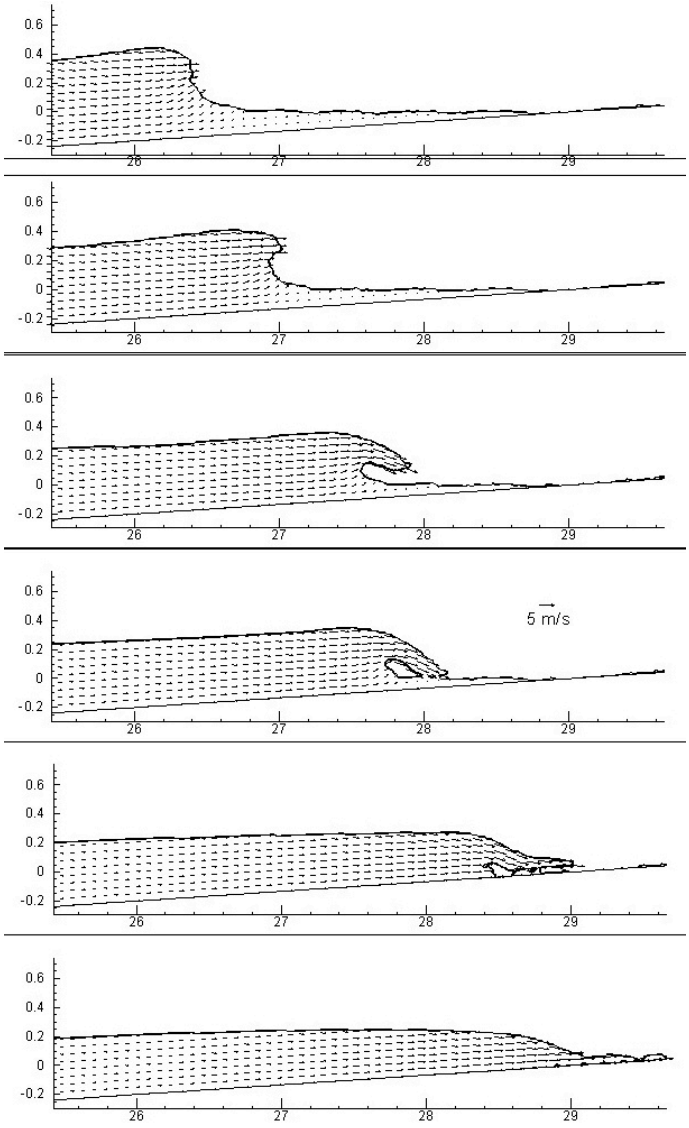

Fig. 6 : Shoaling, breaking and post-breaking for 2D simulations similar to Figs. 4 and 5.

As there are no variations of the slope in the transverse direction, wave breaking is quasi-2D. It is thus interesting to compare 3D results obtained here, in a vertical cross-section along the direction of propagation, with 2D VOF results, e.g., such as computed by Guignard et al. (1999,2001). The 2D computational domain corresponds to a slice of the 3D domain along the propagation direction. The same initial solitary wave is considered and the 2D-SL-VOF method is used (see Guignard et al., 1999, 2001 for details).
The 2D simulation results are shown on Fig. 6. As expected, the same phenomenon occurs, i.e., the creation of large size plunging breaker. Comparisons between the 2D and 3D simulations during breaking are presented on Fig. 7. One can see 2D and 3D simulation results are in close agreement. Small differences are only observed around the wave crest. Also, breaking occurs somewhat faster for the 2D case. This is likely due to effects of discretization, which is coarser in the 3D case and thus causes more numerical errors. Nevertheless, the overall shape of the breaker jets is very similar.

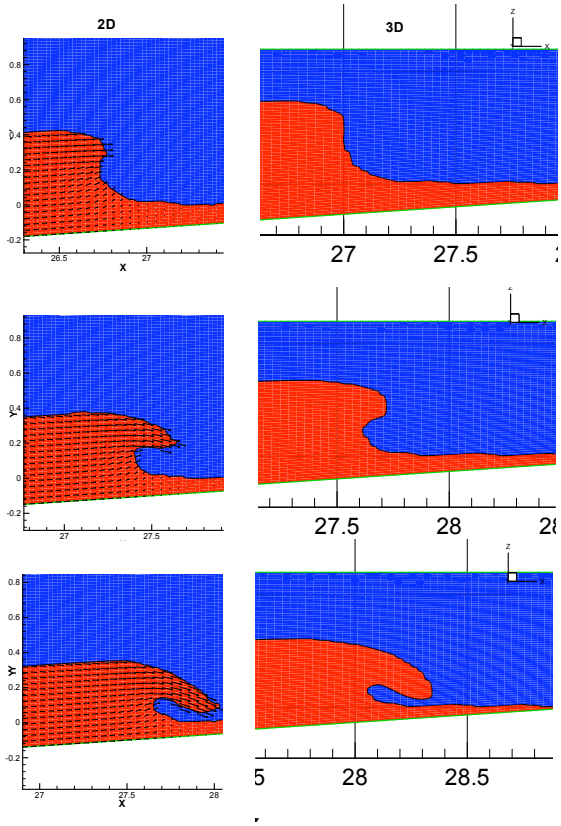

Fig. 7: comparisons between 2-D and 3-D simulations in Figs. 4-6.

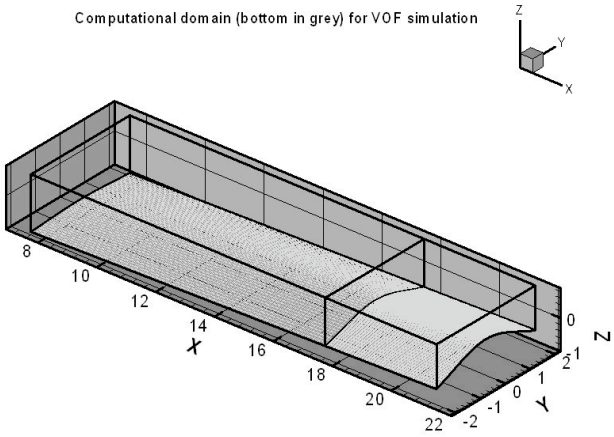

Fig. 8: BIEM/VOF computational domains for solitary wave shoaling over a 3D ridge.

Breaking of a solitary wave over a sloping ridge

The previous test case was computed with the 3D algorithm, but on a quasi 2D configuration. We now compute solitary wave breaking for a case with a fully 3D bottom topography represented by a sloping bottom modulated by a ridge (Fig. 8).

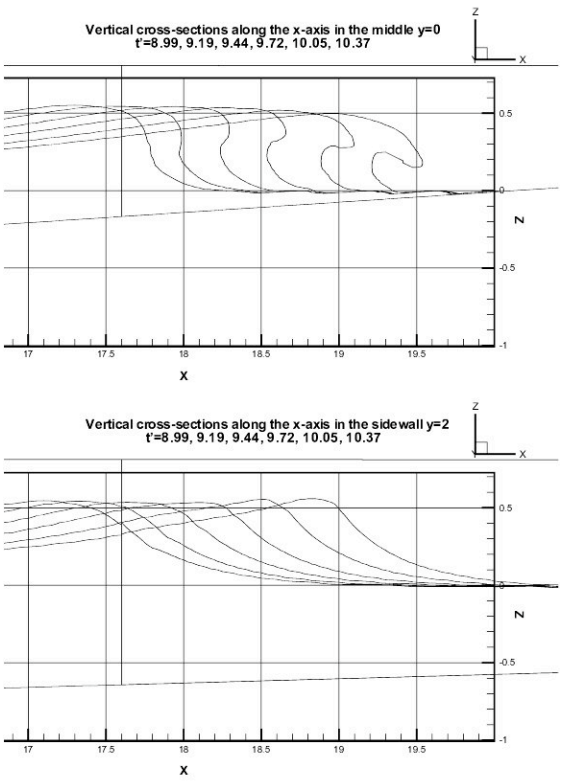

Fig. 9: vertical cross-sections along the x-axis in $y = 0$ and $y = \pm 2$ for computations, in domain of Fig. 8, of the shoaling of a solitary wave of initial height $H' \approx 0.6$.

Computational domain

The domain has a flat bottom (with depth $h_0 = 1$ m), for $x = 1$ to 5.23 m, and a sloping ridge, starting at x=5.23 m, with a 1 : 15 slope in the middle cross-section ($y = 0$) and a transverse modulation of the form sech(ky) ($y = \pm 2$ m, $k = 0.5$), so that the bottom slope is milder on the domain sides (1 : 36; Fig. 8). For the first part of the simulation calculated with the BEM model, the ridge is truncated at $x = 17.6$ m, which eliminates the surface piercing slope and simplifies the BEM discretization. For this case, the initial wave is an exact FNPF solitary wave with $H_0' = 0.6$, and its crest initially located at $x = 5.7$ m. The wave is propagated for time, $t' = t\sqrt{g/h_0} = 0$ to $t' = 6$. The VOF model is initialized for $t' = 6$ in a smaller computational domain, covering $x \in [7.6;21.3]$ and using 352 x 40 x 64 computational cells (Fig. 8). The second phase of computations the VOF method includes additional shoaling and wave overturning. Details are given below.

Overturning stage

As wave shoaling continues in the VOF domain, the bottom variation progressively leads to wave overturning. Due to the shallower depth in the middle of the domain, overturning starts first at $y = 0$ and then propagates laterally. Fig. 9 shows vertical cross-sections of the free surface calculated in the middle ($y = 0$) and at the sidewalls ($y = \pm 2$ m) of the VOF computational domain, for times $t' = 8.99$, 9.19, 9.44, 9.72, 10.05, 10.37. Full 3D views of wave profiles for times $t' = 9.19$, 9.44, 9.72, 10.05 and 10.37 are presented on Fig. 10. The 3D aspects of wave overturning clearly appear on figures 9 and 10. Due to the depth variation over the ridge, the wave profile at $y = 0$ first develops overturning, with a prominent jet, while the surface profiles at $y' = \pm 2$ are still of moderate slope. The wave reaches its maximum height of $H' \approx 0.58$ near the breaking point at $y = 0$. The surface elevation then gradually decreases as the jet of water is projected forward.

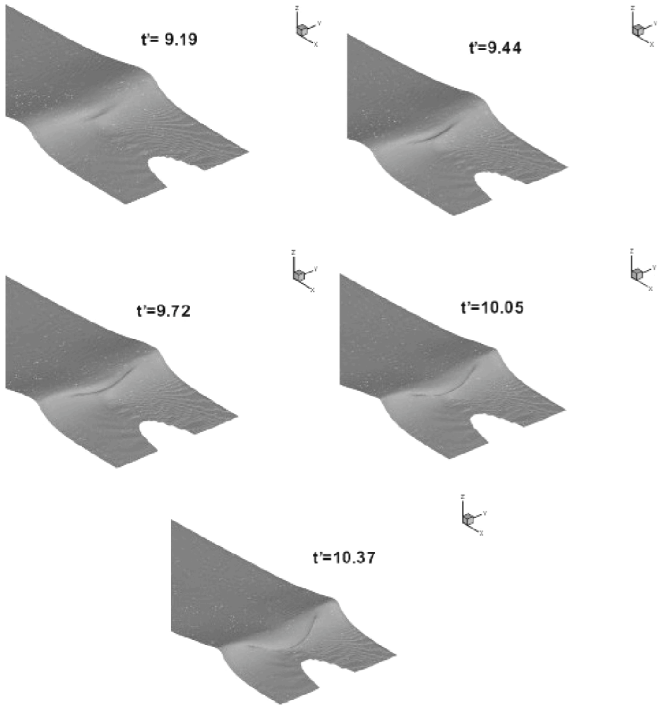

Fig. 10: details of 3-D overturning of the solitary wave of Fig. 9.

Another interesting analysis is to compare the pressure field under the wave at the breaking point to an hydrostatic pressure field based on surface elevation. This allows estimating the applicability of long waves models, which assume hydrostatic pressure (e.g., Nonlinear Shallow Water (NSW) wave models). One can see on Fig. 11 that the ratio between computed pressure and hydrostatic pressure varies between 0.2 and 2.5, for the wave near the breaking point (vertical tangent on the front face). The wave pressure field at the breaking point is clearly far from hydrostatic, especially just in front of the wave, due to large vertical accelerations, neglected in typical long waves model. This observation was also made by Guyenne and Grilli (2002), who used a 3D-FNPF BEM model.

Figure 12 displays the non-dimensional internal velocity field and its non-dimensional magnitude, computed at $t' = 9.82$ and $t' = 10.34$ for $y = 0$, after the wave has passed the breaking point. During breaking, high velocities are observed to occur in the breaker jet, due to high flow convergence. The velocity increases and exhibits more variation in the vertical direction as one enters the breaker jet.

Figure 13 displays the transverse variations of the velocity, due to focusing of the flow by the ridge. Non-dimensional velocities and non-dimensional velocity magnitudes are again shown for $t' = 9.82$ and $t' = 10.34$, at depth $z = -0.2$ m.

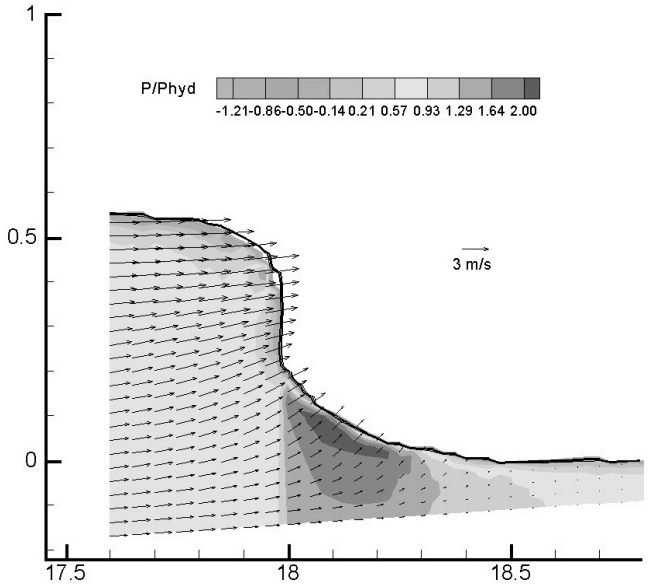

Fig. 11: ratio between computed pressure and hydrostatic pressure for the breaking solitary wave of Fig. 9-10 ($y = 0$).

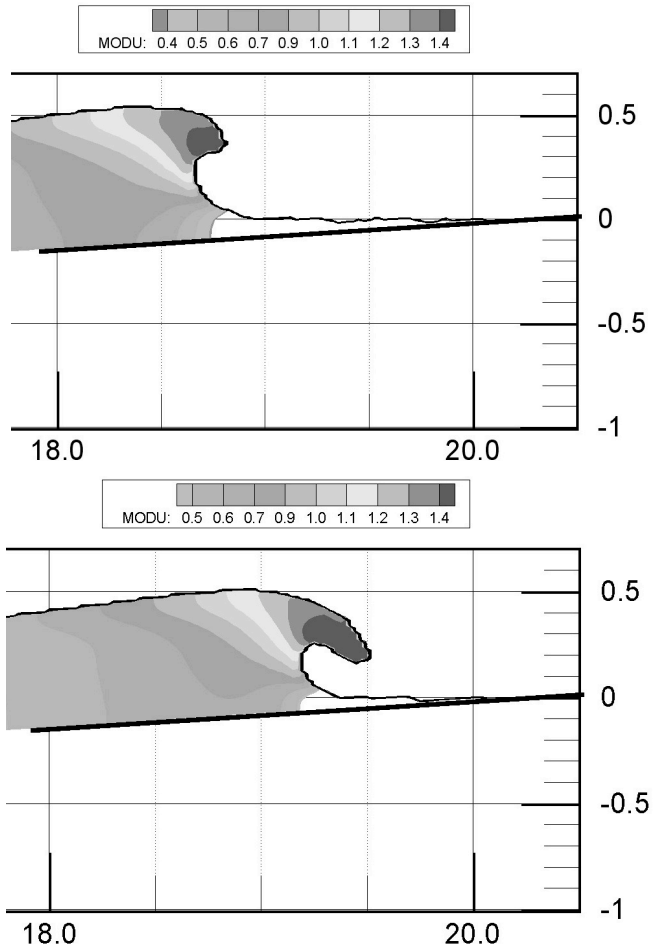

Fig. 12: non-dimensional velocity field (vectors) and magnitude (colors) at $t' = 9.82$ and $t' = 10.34$ ($y = 0$) for results of Figs. 9-11.

Breaking and post-breaking stages

Breaking first occurs at the centre of the 3D ridge and then propagates progressively towards the sides. Fig. 14 displays breaking and post-breaking stages for $t' =$ 10.53, 10.68, 10.82 and 10.89 at the centre of the ridge ($y = 0$). The breaker jet impacts the forward free surface at x = 19.85 m for time $t' =$10.65. The maximum non-dimensional velocity magnitude at this time is 1.63. The wave is submitted to a strong acceleration before breaking. The maximum acceleration magnitude is 4.9 g just before impact.

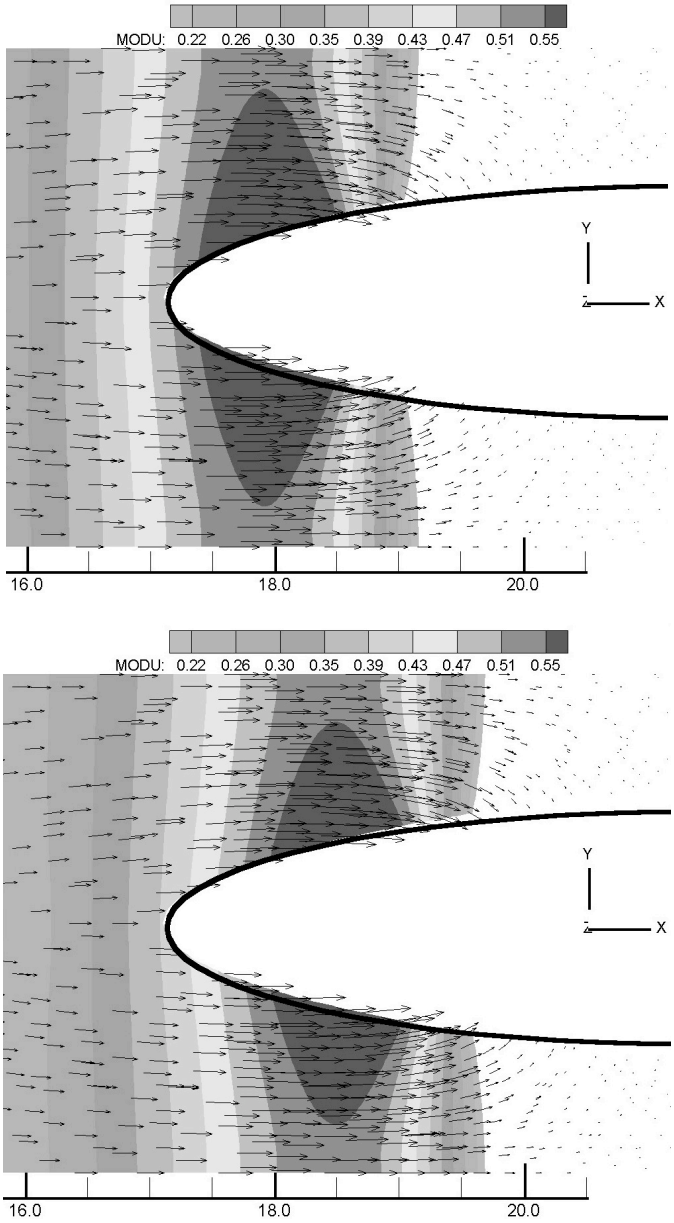

Fig. 13 : transverse modulation of the velocity field (at depth z = -0.2m) for the results of Figs. 9-12.

The 3D aspects of breaking/post-breaking are shown on Fig. 15, where different vertical cross sections along the y-axis are displayed, and in Fig. 16, where full 3D views of breaking are shown. As said before, we clearly see, initially, breaking occurs in the middle part of the wave but not yet on the side parts.

Fig. 17 presents the evolution of vorticity fields in the vertical cross-section at y = 0.4 m, for different non-dimensional times, before and after jet impact. As the impact of the breaker jet occurs in shallow water, only little generation of vorticity is observed. Maximum vorticity is observed to occur at the impact location. In fact, no molecular viscosity or turbulence closure scheme was included in the VOF computations and, based on Kelvin's theorem, since the initial conditions are irrotational, the solution at later times should remain irrotational. Vorticity, however, is generated due to numerical diffusion, which is largest near boundaries, and particularly at the free surface during jet impact (but the modulus of the vorticity vector remains quite small). This can be explained by the use of artificial viscosity in the numerical scheme, in order to uncouple odd and even mesh points. The use of a refined mesh should limit this phenomenon. Nevertheless, this point will have to be further studied and shall be highlighted in future papers. A model accurately including effects of viscosity should also be used to create both stronger and more realistic vorticity fields.

After impact, Fig. 18 shows that the air tube formed by the breaker progressively crashes as the wave continues to collapse in the swash zone. A water jet is then projected with high velocity along the slope. After splash-up, no secondary jet is observed because breaking occurs in shallow water.

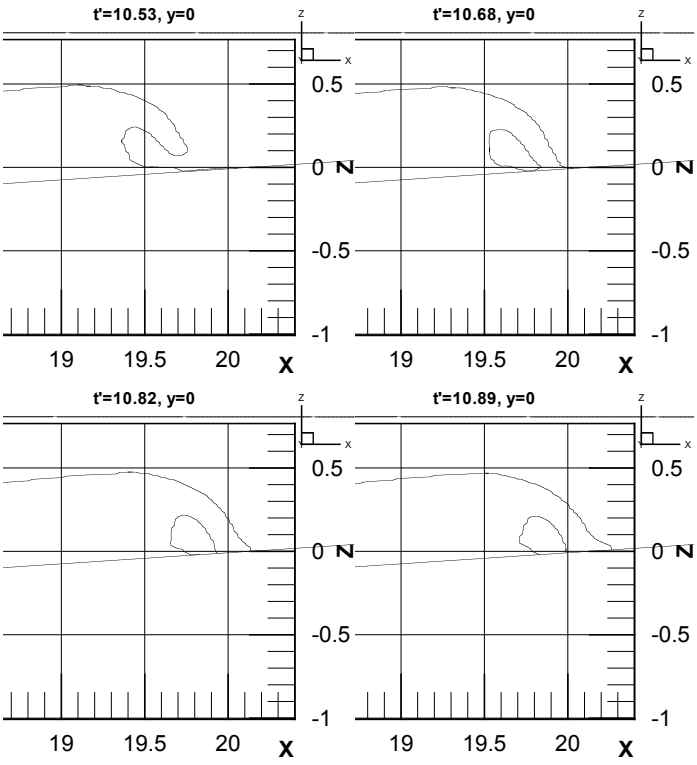

Fig. 14 : Wave breaking/post-breaking at the centre of the ridge for t' = 10.53, 10.68, 10.82 and 10.89 (y = 0) for results of Figs. 9-13.

Numerical performances and comparisons with BEM results

The CPU time for the VOF simulations was five days and ten hours, on a Digital DEC Alpha 500 MHz bi-processor workstation. The numerical error on volume conservation was less than 0.7%. The error on total energy conservation was larger, at about 10%. This can be explained, as briefly discussed above, by the single-phase flow modelling used in the VOF model, in which fields are interpolated on the free surface cells. In the case of a solitary wave, maximum velocities are located at the wave crest, precisely where interpolations are applied. This leads to numerical diffusion and (non-physical) losses of both wave energy and amplitude. [This was also observed by Guignard et al. (1999, 2001), in 2D computations.]

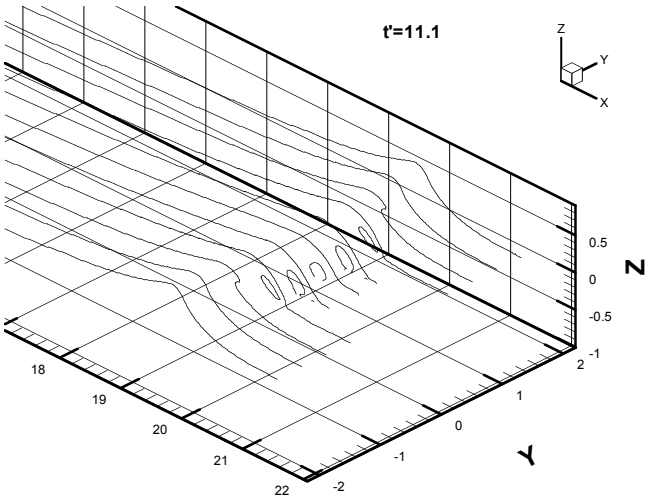

Fig. 15 : Wave breaking at t' = 11.01 for different vertical cross-sections along the x-axis, with Fig. 9-12 results.

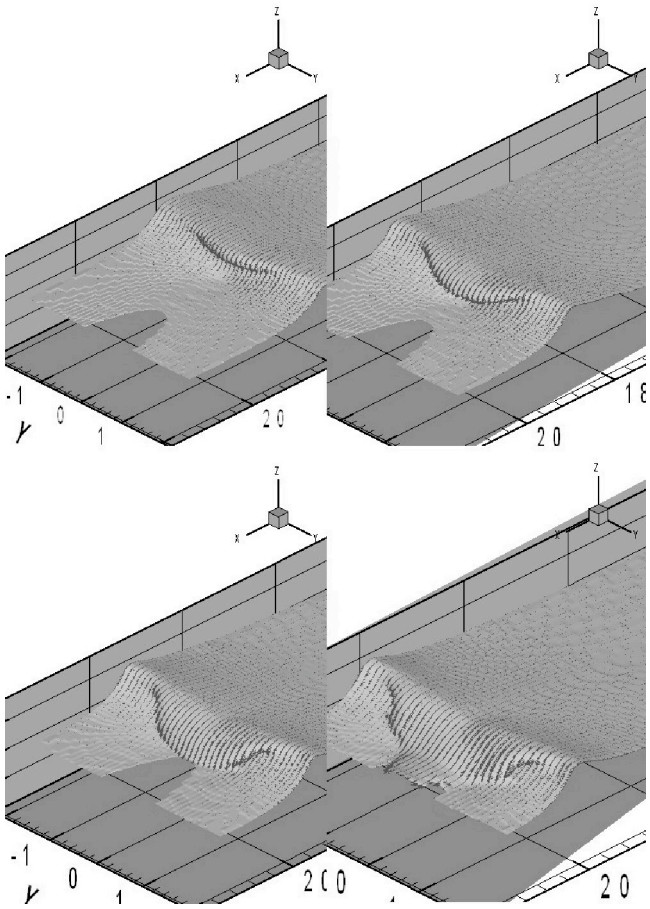

Fig. 16: evolution of breaking (full 3D view) for Fig. 9-15 results.

Comparisons in Fig. 19 between VOF results and Guyenne and Grilli's (2002) BEM results, for waves computed at similar times (t' = 9.182 and t' = 9.196 respectively), and y = 0, 2 m show that wave height at breaking is larger in the BEM results, about 0.7 m, than in VOF results, about 0.58 m.

The numerical loss of energy can also explain the slight time lag observed between the onset of breaking in VOF and BEM results. In Guyenne and Grilli's (2002) computations in Fig. 19, wave energy was very accurately conserved and breaking occurred earlier (at $t' \approx 9$ and $x \approx 18$ m), than in the present computations. Figure 19 also shows that the overturning stage is more developed for similar times in BEM results.

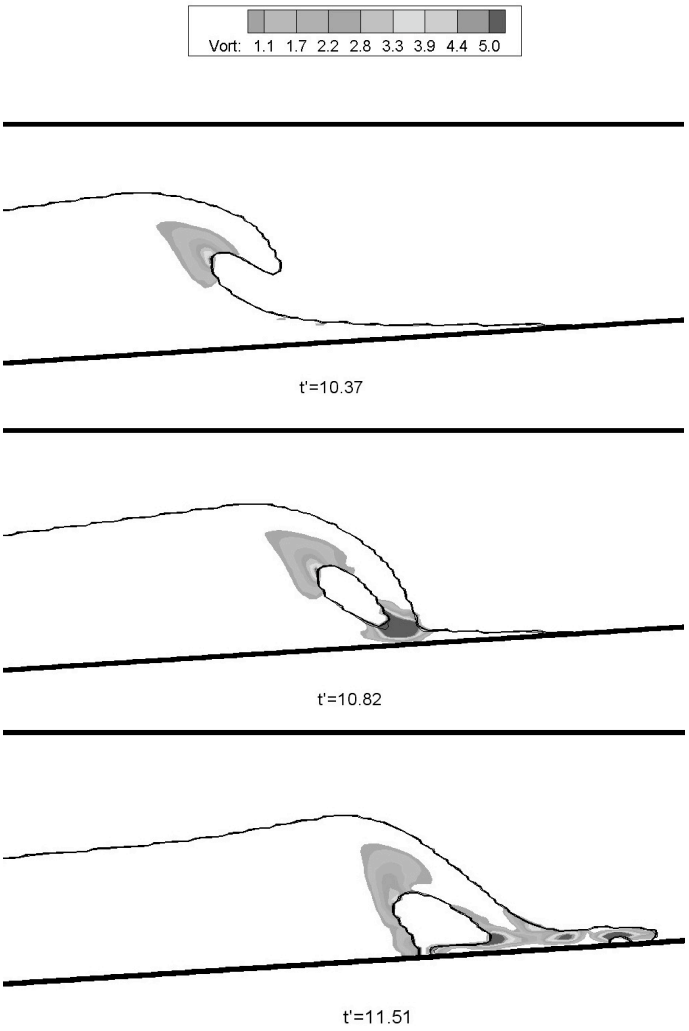

Fig. 17: Vorticity fields in the plane y = 0.4 m, for different non-dimensional times t' in Fig. 9-16 results.

A more detailed analysis of BEM and VOF results displayed in Fig. 19 would show that the maximum computed non-dimensional velocity before jet impact is 1.63 in VOF results and 1.94 in BEM results. The maximum acceleration at this stage is 4.9 g in VOF results and 5.9 g in BEM results (Guyenne and Grilli, 2002). Thus, the wave motion is more dynamic and the computed velocities and accelerations are larger in BEM results than when using the Navier-Stokes/Euler solver.

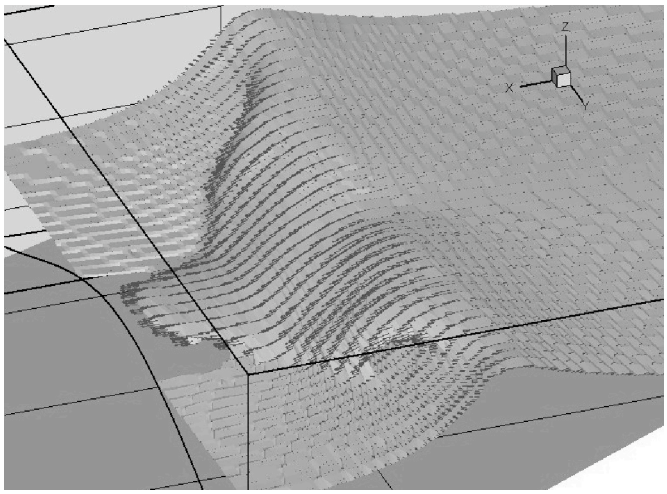

Fig. 18: Wave collapsing and beginning of swash zone for Fig. 9-17 results.

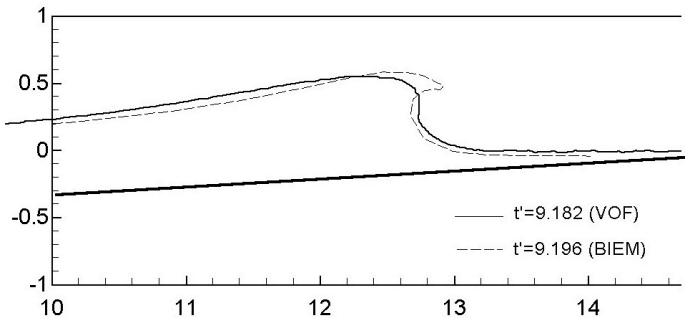

Fig. 19 : comparisons between VOF and BEM results (bottom), for similar t' and y = 2 m (case of Figs. 9-18).

CONCLUSIONS

The coupling between BEM and VOF methods has been used to successfully compute quasi-2D and 3D shoaling, overturning, (plunging) breaking, and post-breaking stages of a large solitary waves. A first test case showed that wave breaking calculated over a sloping bottom agreed well with earlier results of a 2D VOF model. The 3D wave breaking over a sloping ridge with a lateral modulation was calculated next. BEM results computed close to breaking were used to initialize the VOF method on a very refined grid, in which breaking and post-breaking stages, with interface reconnection, were computed.

Three-dimensional effects on wave profile and kinematics were illustrated and discussed. Comparisons with late stages of BEM computations before jet impact showed a loss of wave amplitude and energy in the VOF model, likely due to numerical diffusion near interface in the single phase VOF computations. Despite these differences, the kinematics of the flow and general shape of the wave are consistent with those computed in the more accurate BEM model, up to wave overturning: the focusing on the ridge (especially the 3D effects on transverse velocity), the dynamics, and the aspect of the breaker jet. The VOF results could be improved by the use of two-phase flow model, providing better volume and energy conservation.

This option is available in the numerical model, but remains time consuming for very refined meshes.

In addition to the advantage of using a more efficient and numerically accurate model, such as the 3D-BEM, the lack of vorticity generated in the flow before jet impact (Fig.10), further supports the relevance of using potential flow theory to model wave transformation up to near breaking.

Future improvements of the VOF model should include using viscosity (because only little vorticity is generated here after breaking), with a proper representation of dissipation at sub-grid scales. Although two-phase flow modelling is costly, boundary conditions on the interface would be more accurately represented. This should help reduce wave energy loss before breaking.

ACKNOWLEDGEMENTS

The authors wish to acknowledge support from the French National Program PATOM (Programme Atmosphère et Océan à Multi-échelles). The second author (S.T.G.) acknowledges support from the US National Science Foundation, under grant CMS-0100223 of ``the Engineering/Earthquake, Hazards and Mitigation Program".

REFERENCES

Biausser, B., Guignard, S., Marcer, and R., Fraunié, P. (2001). "Numerical simulations of free surface flows using a new VOF method," *Proc. 4th Seminar Euler and Navier-Stokes Equations, Institute of Thermomechanics,* Prague.

Biausser, B., Guignard, S., Marcer, and R., Fraunié, P. (2004). "3-D two-phase flows numerical simulations by SL-VOF method", *Int. Jour. For Num. Meth. In Fluids,* Vol 45, pp 581-604.

Brandini, C. and S.T., Grilli (2001). "Modeling of freak wave generation in a 3D-NWT, " *In Proc. 11th Offshore and Polar Engng. Conf.* (ISOPE01, Stavanger, Norway, June 2001), Vol III, pp 124-131.

De Jouëtte, C., Viviand, H., Wornom, S. and Le Gouez, J.M. (1991). "Pseudo-Compressibility Methods for Incompressible Flow Calculation," *Proc 4th International Symposium on Computational Fluid Dynamics*, University of California, Davis.

Grilli, S.T., Guyenne, P. and Dias, F. (2001). "A fully nonlinear model for three-dimensional overturning waves over arbitrary bottom," *Intl J. Numer. Meth. Fluids* , Vol 35, No 1, pp 829-867.

Grilli, S.T. and Horrillo, J. (1997). "Numerical Generation and Absorption of Fully Nonlinear Periodic Waves," *J. of Engng. Mechanics*, Vol. 123, No. 10, pp 1060-1069.

Grilli, S.T. and Horrillo, J. (1999). "Shoaling of periodic waves over barred-beaches in a fully nonlinear numerical wave tank," *Intl. J. Offshore and Polar Engng.*, Vol. 9, No. 4, pp 257-263.

Grilli, S.T., and Subramanya, R (1996). "Numerical modeling of wave breaking induced by fixed or moving boundaries," *Computational Mech.*, Vol 17, pp 374-391.

Grilli, S., Subramanya, R., Svendsen, I.A. and Veeramony, J. (1994). "Shoaling of Solitary Waves on Plane Beaches." *J. Waterway Port Coastal and Ocean Engng.*, Vol 120, No 6, pp 609-628.

Grilli, S.T., Svendsen, I.A. and Subramanya, R. (1997). "Breaking Criterion and Characteristics for Solitary Waves on Slopes." *J. Waterway Port Coastal and Ocean Engng.*, Vol 123, No 3, pp 102-112.

Guignard, S., Grilli, S.T., Marcer, R. and Rey, V. (1999). "Computation of shoaling and breaking waves in nearshore areas by the coupling of BEM and VOF methods." In *Proc. 9th Offshore and Polar Engng. Conf.* (ISOPE99, Brest, France, May 1999), Vol. III, pp 304-309.

Guignard, S., Marcer, R., Rey, V., Kharif, Ch. and Fraunié, P. (2001). "Solitary wave breaking on sloping beaches:2D two-phase flow numerical simulation by SL-VOF method". *Eur. J. Mech. B/Fluids,* Vol. 20, pp 57-74.

Guyenne, P., and Grilli, S.T. (2004). "Numerical study of three-dimensional overturning waves in shallow water" (submitted).

Hirt, C.W., and Nichols, B.D. (1981). "Volume Of Fluid Method for the dynamics of free boundaries," *J.Comp. Phys.,* Vol 39, pp 323-345.

Lubin, P., Vincent, S., Caltagirone, J.-P. and Abadie, S. (2003). "Fully Three-dimensional Direct Numerical Simulation of Plunging Breaking Waves", *C. R. Mécanique*, **331**, 495-501.

Tanaka, M. (1986). "The stability of solitary waves," *Phys. Fluids,* Vol 29, No 3, pp 650-655.

Viviand, H. (1980). "Pseudo-unsteady Methods for Transonic Flow Computations," *19th International Conference on Numerical Methods in Fluid Dynamics*, Stanford, i*n Lecture Notes in Physics,* Vol. 141, Springer-Verlag, New-York.

Viviand, H. (1995). "Analysis of pseudo-compressibility systems for compressible and incompressible flows," *Comp. Fluid Dynamics Review,* Hafez-Oshima editor, Wiley publishers, pp.399-418.

Xü, H, and Yue, D.K.P. (1992). "Computations of fully nonlinear three-dimensional water waves," *Proc. 19th Symp. On Naval Hydrodynamics*, Seoul, Korea.